Experimental Thermal and Fluid Science 119 (2020) 110215

Contents lists available at ScienceDirect

Experimental Thermal and Fluid Science

journal homepage: www.elsevier.com/locate/etfs

Visualization and measurements of shock waves in cavitating flow

Martin Petkovšek, Marko Hočevar, Matevž Dular*

Laboratory for Water and Turbine Machines, Faculty of Mechanical Engineering, University of Ljubljana, Aškerčeva 6, 1000 Ljubljana, SI, Slovenia

ARTICLE INFO

Keywords:
Cavitation
Shock waves
High speed video
Cloud collapse

ABSTRACT

Upon cavitation cloud collapse an omnidirectional shock wave is emitted. It then travels through the flow field, causing a cascade of events resulting in erosion, noise, vibration and the cavitation shedding process.

Despite that the accumulated data points evidently to the presence of the shock waves, the direct measurements hardly exist - and even then, they are very expensive and time consuming to perform.

In the present paper, the possibility of detecting shock waves inside cavitating flow is shown.

The methodology bases on using two conventional high speed cameras. With the first one cavitating flow from a distance is observed, determining the position of the wave, while the second camera with a microscopic lens enables a close-up view to determine the number and size change of air bubbles as a shock wave passed them. By calibration and reference measurements the amplitude of the shock waves was determined.

This relatively simple approach enabled the first observation of shockwaves which occur at the cavitation cloud collapse (downstream of the attached cavity). Several examples of shock wave dynamics are shown and how they influence the general cavitation cloud behaviour. Shock wave front velocities and local pressure waves caused by cloud collapse were estimated from visualization, reaching values to more than 700 m/s and over 5 MPa respectively.

1. Introduction

Cavitation is characterized as inception, growth, and collapse of vapour-gas bubbles, due to the local change in the pressure. In many cases, it is an unavoidable and undesirable phenomenon in hydraulic machinery, as it causes vibration, noise, deterioration of efficiency and even erosion of the elements of the flow tract.

Developed hydrodynamic cavitation with periodic shedding of vaporous structures (Fig. 1) is one of the several cavitation types which can form in the low-pressure region of the flow tract. It is acknowledged, that two mechanisms govern the shedding process:

- Re-entrant jet. Due to the differences in the pressure inside and outside of the attached cavity, the flow, which passes it, deviates towards the surface of Venturi (or any other submerged object, i.e. hydrofoil or pump/turbine blade) [1,2]. This builds a stagnation point just downstream of the attached cavity closure line. The flow then separates in downstream and upstream part - the latter enters the attached cavity and upon losing the momentum, causes its separation - forming a detached cavitation cloud, which carries a significant amount of potential energy. As the cloud is carried downstream, it enters a higher pressure region, due to which it collapses and emits shock waves in the order of MPa [3].
- Shock wave. This mechanism was observed recently during X-ray densiometry [4,5]. It was found that the collapse of the cavitation cloud causes a shock wave that spreads through the flow field. As it travels upstream, inside a highly compressible two-phase mixture, it slows down to a velocity in the order of several m/s, while still moving at a (super)sonic speed. The passage of the shock suppresses the attached cavity, which firstly shrinks. When the discontinuity in void fraction reaches the region of cavity detachment at the wedge apex, a large vapour cloud is shed. Later on the cavity begins to grow.

The two mechanisms resemble each other, one apparent difference is the somewhat smaller size of detached cavitation clouds in the case of re-entrant jet driven process (Fig. 1).

Fig. 1 shows typical cavitation dynamics, which was encountered during the present study. Also, the corresponding acoustic spectrum is shown. We can observe periodic shedding of large cavitation clouds. Likely we are dealing with predominately re-entrant jet mechanism, since only a part of the attached cavity (from closure up to its mid-length) pinches off [4]. The attached cavity grows until t = 1.67 ms. From this moment onwards, liquid begins to flow upstream beneath the vaporous pocket (t = 2.08 ms). As it loses momentum it turns upwards and causes the separation of a large cavitation cloud (t = 2.50 ms): The cloud is then convected downstream, where it collapses at t = 4.58 ms.

* Corresponding author.
E-mail address: matevz.dular@fs.uni-lj.si (M. Dular).

https://doi.org/10.1016/j.expthermflusci.2020.110215
Received 6 April 2020; Received in revised form 1 June 2020; Accepted 24 June 2020
Available online 06 July 2020

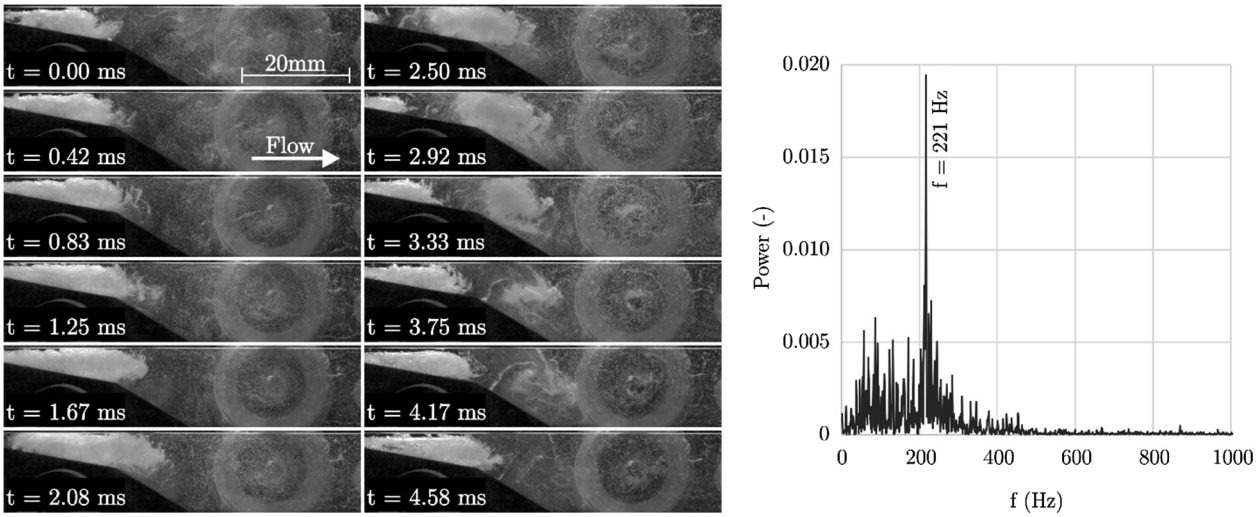

Fig. 1. Periodic shedding of cavitation structures in the present configuration and the corresponding acoustic spectrum.

The process is then periodically repeated. The concentric rings seen in the right side of each image are the pressure transducer and its mounting into the back side of the channel (they do not interfere with the flow field).

The existence of shock waves cannot be disputed as it was proven by a number of numerical studies and local pressure measurements [6–8]. Furthermore, they are the needed condition of the occurrence of cavitation erosion.

The most evident measurements were done on single bubble cavitation. Here the bulk flow is liquid and schlieren or a similar technique can easily be applied.

Petkovšek et al. [9] observed laser-induced breakdown in water. The formation and the propagation of the shock wave were monitored by a beam-deflection probe and an arm-compensated interferometer. The time-of-flight data from the breakdown site to the probe beam yielded the velocity, and from the velocity, the shock-wave pressure amplitudes were calculated. Further on, they used simultaneous measurements based on shadow photography as a comparative method for their experiments [10].

Supponen et al. [11] recently presented detailed observations of the shock waves emitted at the collapse of single cavitation bubbles using simultaneous time-resolved shadowgraphy and hydrophone pressure measurements. They show that nonspherical collapse produces multiple shocks that are clearly associated with different processes, such as the jet impact and the individual collapses of the distinct bubble segments.

The conditions inside cavitating flow are much more complex, hence pressure field measurements hardly exist. Brennen et al. [12] were the first to use piezoelectric transducers, mounted at several locations, to determine the amplitudes of the pressure waves from the cavitation cloud collapse.

Other researchers, for example, Brujan et al. [13] resort to “synthetic” bubble cloud generation by ultrasound and use high speed video techniques to capture the pressure peaks.

An innovative approach, which was partially followed in the present study, was introduced by Sugimoto et al. [14]. For the case of impinging cavitating jet, they used high speed video observation and the frame difference method. By this simple approach, they could resolve the behaviour of pressure waves. The same method was also adopted by Waldrop & Thomas [15] for the case of a convergent-divergent nozzle, but in their case air bubbles needed to be introduced to resolve the shocks.

Evidence is equally supportive from the results of simulations. Budich et al. [7] successfully reproduced a majority of features that were measured by Ganesh et al. [4] - including condensation shocks, which lead to the periodic behaviour of cavitation. Rasthofer et al. [16] were the first to numerically resolve individual bubbles inside a large cavitation cloud. By performing a largescale simulation of a collapse of a completely resolved cavitation cloud, they were able to confirm most of the flow features predicted by the experimentalists (shock waves, jetting, coalescence). On the other hand, even simpler (RANS) simulations, which take into account the compressibility effects of two phase flow, still contribute to the general understanding of the effects of cavitating flow [17].

In contrast to the studies by Sugimoto et al. [14] and Waldrop & Thomas [15] we use “pure”, not ventilated, cavitating flow and use solely observation of the main features (simultaneous observation of the whole flow field and microscopic observation of bubbles inside a focused region of interest) of the flow to determine both the dynamics and the amplitude of the pressure waves. Also we are not focusing on the presence of the condensation shocks in high void fraction regions of the flow and its influence on the main shedding mechanism, as Ganesh et al. [4], but rather to the shock wave dynamics in the region where the bubbly clouds collapse.

We first show the experimental set-up (Section 2), then we move on to the description of the image analysis technique and the formulation, which was used to determine the amplitude of the shocks (Section 3). Results, showing several examples of shock waves, their interaction with the main flow and their interaction with each other are given in Section 4. The conclusions are presented in Section 5.

2. Experimental set-up

Tests were performed in a small cavitation tunnel which is primarily used for studies of cavitation exploitation [18].

Cavitation tunnel (Fig. 2 - left), firstly described in [19], is based on a symmetrical Venturi constriction, connected with two equal reservoirs, where the flow is induced by a pressure difference between them.

Double angle (10° and 30°) divergent Venturi nozzle (Fig. 2 - right) was designed in order to achieve more rapid pressure recuperation downstream the Venturi throat. This causes a more violent collapse of cavitation structures, resulting in high density energy release, which helps in generation of shockwaves. The Venturi nozzle throat width and height equalled 5 mm and 1 mm, respectively. The entire section was made with transparent acrylic glass in order to enable visualization of cavitation inside the Venturi channel from various angles.

Measurements were performed by visualization and pressure fluctuations measurements. Visualization was performed by two high-speed cameras, synchronised and triggered simultaneously. Photron FastCam SA-Z was used to obtain the overall view of cavitation. Photron FastCam Mini AX-200 was fitted with microscopic lens to capture detailed view of cavitation bubbles in a small region of interest. For the presented experiments the frame rate of 120,000 fps was used - the

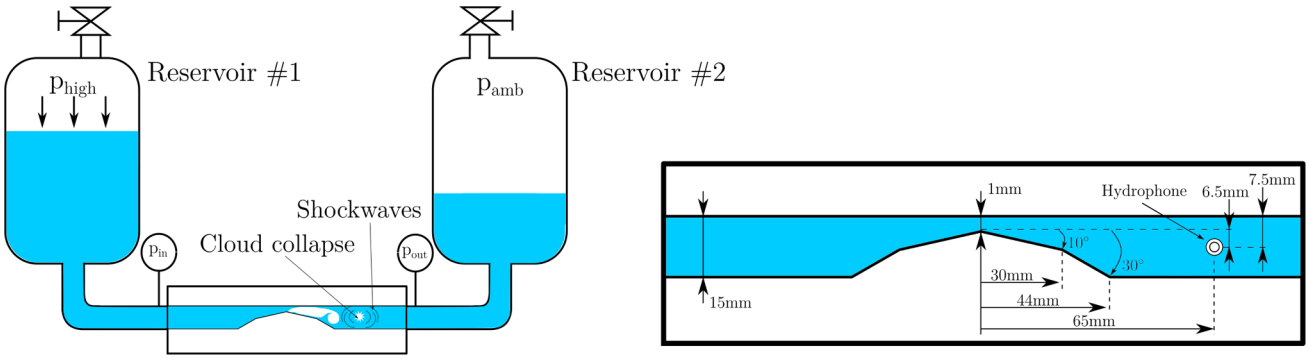

Fig. 2. Experimental Set-up (Cavitation tunnel – left, Test section – right).

resolution was 768 × 176 pixels (80 µm/pixel) for integral and 256 × 128 pixels (15 µm/pixel) for detailed view. High power LED illumination allowed to set a very short shutter time of 2.5 µs for both overall and detailed view.

Pressure oscillations were measured by a hydrophone ResonTC4013 with usable frequency range 1 Hz to 170 kHz and receiving sensitivity of −211 dB ± 1 dB re 1 V/µPa. The hydrophone was used with Reson EC6081 amplifier. The hydrophone was mounted 65 mm behind and 6.5 mm below the throat.

Every flow, cavitating or not, can be attributed by a cavitation number (Eq. (1)), its value depends on the pressure at the inlet to the Venturi section p_{in} (positions of the pressure measurements are shown in Fig. 2 - left), flow velocity v, vapour pressure p_v and density of the liquid ρ:

$$\sigma = \frac{p_{in} - p_v}{\frac{1}{2}\rho v^2} \tag{1}$$

Eq. (1) can be also formulated with the pressure difference [20]:

$$\sigma = \frac{p_{in} - p_v}{\Delta p} \tag{2}$$

where Δp is the pressure difference between inlet and outlet of the constriction ($\Delta p = p_{in} - p_{out}$). The latter formulation enables the determination of cavitation number without knowing the exact velocity of the flow.

2.1. Experiment

Experiments were conducted under the same operating conditions for all presented results in the paper. During the experiments the fresh tap water (used liquid) temperature equalled 21 °C and did not deviate more than 2 °C. The amount of dissolved oxygen during the experiments equalled 7.25 mg/L ± 0.2 mg/L (measured with O_2 probe Intellical LD0101 on HachLange HQ430D multimeter instrument).

Operating conditions for cavitation tunnel were set to have 6 bar of absolute static pressure at the inlet (p_{in}) and 1.1 bar of absolute static pressure at the outlet (p_{out}) – due to local pressure losses the outlet pressure exceeded ambient pressure (0.98 bar). From Eq. (2) the cavitation number can be determined and equals $\sigma = 1.22$ (noting a reasonably developed cavitating conditions).

3. Methodology

As mentioned, two synchronised high speed cameras were used to observe the flow field. One recorded the whole region of interest while the other recorded only a small part (4 × 2 mm), but at a much higher resolution. Different local regions of interest were observed during the experiments.

Fig. 3 shows an exemplary sequence recorded by both cameras.

It is nearly impossible to see the passage of the shock wave in the left (low resolution/integral) sequence – a close observation reveals that a “darker region” moves at a high velocity from the left to the right. This is caused by the slight change of light scattering on the bubbles and light attenuation by the bubbles, which change in size due to the passage of the shock wave. This can be better seen in the right (high resolution) sequence, where individual bubbles can clearly be resolved. As the shock passes them, they shrink in size, what can be seen at t = 50 µs and at t = 67 µs. Both types of sequences, together with the pressure transducer data, were later used for reference measurements and for visualization and quantification of shocks, which occur in the section. This is further elaborated in Section 3.3.

3.1. Shock wave measurement

As the shock wave passes a bubble, the bubble shrinks in size. On a macroscopic level, inside the bubbly flow, this can be seen as a slight decrease in image intensity (Fig. 3, left). A $n \times m$ pixel image at time t can be represented as a matrix with $n \times m$ elements, which can, in an 8-bit system, occupy levels A from 0 (black) to 255 (white) ($A \in \{0 \cdots 255\}$). The change in intensity can be simply determined by subtracting (or dividing) two consecutive images.

The issue we are faced with is that by subtraction (or division) of two consecutive images all the changes in the light intensity in the image are revealed - that is both those due to the passage of the shock wave and those due to the passage of the cavitation clouds by the flow convection. The latter needs to be appropriately considered and neglected. The technique is described in the following section.

3.1.1. Local convection velocity

Local flow velocity is determined from the sequences of the images. Since we are interested solely in the convection of the structures we employed the methodology presented by Bizjan et al. [21]. The velocity calculation algorithm bases on a simplified advection–diffusion equation (Eq. (3)):

$$\frac{\partial C}{\partial t} + \frac{\partial (C v_x)}{\partial x} + \frac{\partial (C v_y)}{\partial y} = D\left(\frac{\partial^2 C}{\partial x^2} + \frac{\partial^2 C}{\partial y^2}\right) \tag{3}$$

D represents the diffusion coefficient of the liquid phase, while v_x and v_y are the local components of velocity. C is the concentration, which in the present case corresponds to the bubble number density and is assumed to be proportional to the intensity of grey level (image intensity) in the region of interest. Derivatives are discretized using the central difference method. In essence, we are solving Eq. (3), but without boundary conditions there are more unknowns than equations. To close the system of equations combined temporal and spatial smoothing were used with the image downsampling. The temporal smoothing penalizes rapid temporal changes in velocity fields, having an effect of a moving average filter over the unfiltered 2D time series of velocity fields. The spatial smoothing on the other hand penalizes high velocity gradients in the calculation domain, working as a low-pass filter and at the same time allowing a reduction in the number of

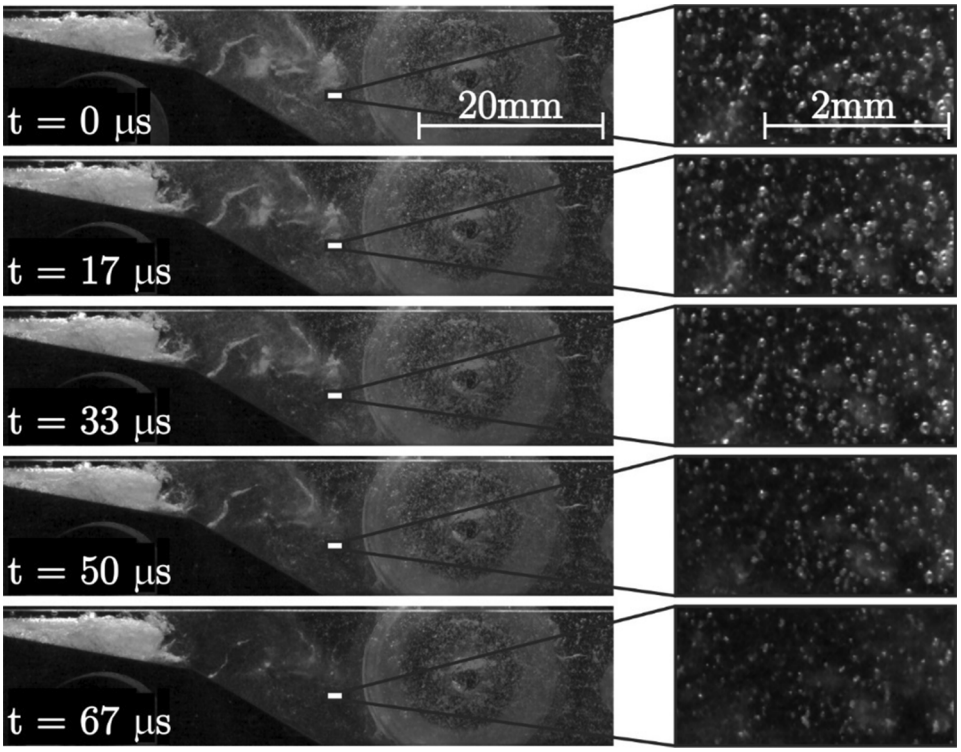

Fig. 3. A series of enhanced images showing the passage of the shock wave. The left series was recorded at a low resolution and the right one with the high resolution. Both series were synchronised.

unknowns in the system of equations. Both filters act in our favour since the rapid movement of shock waves is filtered, while slower convection of the structures is not. The final solution of the equation system is obtained using the least squares method. Details about the velocity calculation algorithm can be found in [21].

A typical velocity filed is shown in Fig. 4.

The velocity, or shift, field tells us the required translation of each pixel in order to diminish the effect of vapour convection. The required shift is in an order of 3 pixels in the x and 1 pixel in the y direction. The process is explained in the following section.

3.1.2. Time derivative of light intensity

The original image matrices for $t + \Delta t$ were transformed to take into an account the local convection ($\Delta x(m, n)$ and $\Delta y(m, n)$) of the cavitation structures (Eq. (4)):

$$Img(t + \Delta t) = \begin{bmatrix} A(1 + \Delta x_{1,1}, 1 + \Delta y_{1,1}, t + \Delta t) & \cdots & A(1 + \Delta x_{1,n}, 1 + \Delta y_{1,n}, t + \Delta t) \\ \vdots & \ddots & \vdots \\ A(m + \Delta x_{m,1}, 1 + \Delta y_{m,1}, t + \Delta t) & \cdots & A(1 + \Delta x_{m,n}, 1 + \Delta y_{m.n}, t + \Delta t) \end{bmatrix} \quad (4)$$

The change (time derivative) in image intensity $\dot{A}$ is then:

$$\dot{A}(t) = \frac{Img(t + \Delta t) - Img(t)}{\Delta t} \quad (5)$$

The passage of the shock wave results in the local decrease of the bubble size. In images, this reflects in a negative value of derivatives of A ($\dot{A}(t) < 0$) - in the case where the light intensity at $t + \Delta t$ was smaller than the light intensity at t. Hence, we need to focus only on the negative values of $\dot{A}(t)$ to determine the position of the shock wave.

3.1.3. Shock wave amplitude

To estimate the amplitude of the shock wave a simple approach was used. Comparing the characteristic time of heat transfer and the time of bubble collapse, we find them to be in the same order of magnitude, hence the process is mainly compression/expansion driven [22]. Also, because the liquid was saturated by gas, we assume that the radius of the free bubble is stable. The pressure inside the bubble p_B is given by Eq. (6):

$$p_B = p_\infty + \frac{2\sigma}{R} \quad (6)$$

where p_∞ is the pressure outside the bubble, σ is the surface tension and R is the radius of the bubble. The same pressure, p_B, can also be expressed as the sum of partial pressures of vapour p_∞ and gas p_g (Eq. (7)):

$$p_B = p_v + p_g = p_v + p_{g,0}\left(\frac{R_0}{R}\right)^{3\kappa} \quad (7)$$

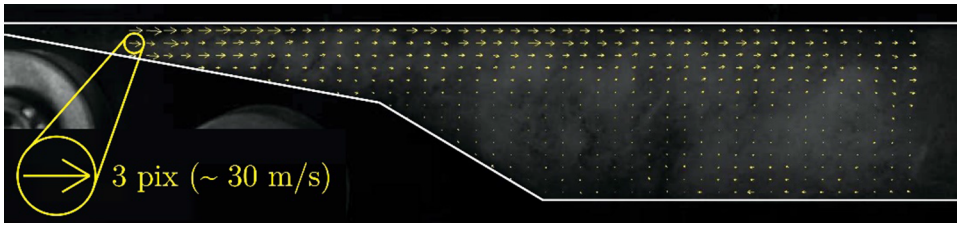

Fig. 4. An instantaneous velocity (shift) field.

In Eq. (7), $p_{g,0}$ represents the gas pressure at a reference bubble radius R_0, which needs to be adjusted for the change in radius according to the polytropic law (κ is the polytropic constant).

Rearranging Eq. (6) and combining it with Eq. (7), gives us the pressure outside the bubble:

$$p_\infty = p_B - \frac{2\sigma}{R} = p_v + p_{g,0}\left(\frac{R_0}{R}\right)^{3\kappa} - \frac{2\sigma}{R} \tag{8}$$

We still need to determine the reference partial gas pressure inside the bubble $p_{g,0}$. We get this from the reference pressure outside the bubble $p_{\infty,0}$ and the bubble radius at that pressure R_0:

$$p_{\infty,0} = p_v + p_{g,0}\left(\frac{R_0}{R_0}\right)^{3\kappa} - \frac{2\sigma}{R_0} = p_v + p_{g,0} - \frac{2\sigma}{R_0} \tag{9}$$

or rearranged:

$$p_{g,0} = p_{\infty,0} - p_v + \frac{2\sigma}{R_0} \tag{10}$$

Finally, we introduce Eq. (10) into Eq. (8) to obtain the final expression for the local pressure:

$$p_\infty = p_v + \left(p_{\infty,0} - p_v + \frac{2\sigma}{R_0}\right)\left(\frac{R_0}{R}\right)^{3\kappa} - \frac{2\sigma}{R} \tag{11}$$

Equation 11 depends solely on constants - on a reference measurement that reveals the relationship between pressure outside the bubble $p_{\infty,0}$ and the bubble radius at that pressure R_0 - and on time dependent measurements of local bubble size R.

4. Results

4.1. Reference measurements

To calibrate the technique, we mounted a pressure transducer downstream of the throat of the Venturi (see Fig. 2 and also Fig. 3). Pressure oscillations were measured by a hydrophone as discussed in section 2. At the same position we captured detailed images of and, in addition, lower resolution images of the whole flow field. All three devices (pressure transducer and the two cameras) were synchronised.

Fig. 5 shows the bubbles response to the passage of the shock wave. To localize and measure the number and size of bubbles in the images, an algorithm was developed - as a result the bubbles in the sequence on the right are encircled (red).

At the beginning of the sequence the measured pressure is low (a). As the shock approaches the bubbles begin to shrink (b and c) and reach the smallest size at the moment of the highest measured pressure (from pressure transducer) – instant (d), as the shock passes the region of interest the pressure drops and the bubbles grow back (e). At an instant (f) the transducer records a slight increase in pressure, which is a result of a shock reflection. Later-on the pressure stabilizes and the bubbles occupy a stabile size (g and h).

From the high resolution images, we are able to determine the distribution of sizes of the bubbles as a function of time. Here also a possibility of overlapping bubbles was considered. The principle that is used is that a single bubble cannot form a concave shape [23]. Hence, a concavely shaped region, which is deemed as several bubbles, is divided into a number of individual objects each having a convex shape. The separated objects are then enlarged to fill out the original object size. Fig. 6, which corresponds to the diagram in Fig. 5, shows time dependent histograms of bubble size distribution. The dotted line shows the average size of the bubble.

The shock wave passes at $t = 0.20$ ms. Both the number of the bubbles and the size decrease. Larger bubbles became smaller and the diameter of initially small bubbles decreased below the camera resolution. Likely, after the collapse of bubbles, nuclei remain the region and contribute to subsequent bubble growth – this is also the reason why the distribution of bubble size and number after the passage of the shock wave closely resembles the one prior to the passage (observing $t = 0.14$ ms and $t = 0.27$ ms in Fig. 6). The bubble number can therefore be taken as a constant. At $t = 0.25$ ms, when we recorded the reflection of the pressure wave (Fig. 5, instant f), one can see a very slight shift of the bubble size distribution towards the smaller radii (this is best noted when a dotted line (average bubble size) is observed). The bubbles respond quickly to the rapid change of the local pressure, and they can be used to determine the shock wave dynamics and even amplitude.

From the high-resolution images the size of the bubbles and count their number were measured. Because the section is thin enough, we can observe bubbles in the whole span of the section. This gives us a unique possibility to determine the local void fraction – a feature which is normally not available with conventional imaging due to light scattering and absorption [4]. The local void fraction is therefore simply:

$$\alpha = \frac{\sum_{i=1}^{N}\left(\frac{4}{3}\pi R_i^3\right)}{V} \tag{12}$$

with N being the number of bubbles, R_i the radius of the individual bubble, and V the control volume – 40 mm^3 (length × height × width − 4 × 2 × 5 mm).

A further step, that we consider was to correlate the high-resolution images, from which void fraction can be measured to the low-resolution images – grey level vs. α. Fig. 7 shows the correlation, obtained from a sample of 1200 image pairs.

For the present case a polynomial correlation with $R^2 = 0.951$ was obtained. This correlation is only valid for this specific test configuration and cannot be applied to other configurations. In the present case it is high enough that we are confident to use the low-resolution images as an input to determine the local pressure, based on Eq. (11). We assume:

$$R \propto f(graylevel) \tag{13}$$

Relation given in Eq. (13) is valid only in certain limits ($0 < \alpha < 35\%$) and equally important, only if the number of the bubbles remains constant (again, looking at Fig. 6 it is unlikely that the bubbles would simply disappear, as they do reappear after the passage of the shock).

Fig. 8 shows the comparison between the shock wave amplitude measured by the pressure transducer and the one obtained from the image analysis (again for the case of sequence in Fig. 5).

The fit between both sets is evident. We are able to reconstruct the pressure evolution (in time and in amplitude), even the slight pressure increase at the passage of the reflected shock wave (at approximately t = 0.25 ms). We feel that the method is sufficiently accurate to perform further analysis on the whole flow filed. The results for specific cases are given in the next section.

4.2. Shockwave visualization

In the following, several cases of shockwave visualization in situations, which frequently occur during the cavitation cloud shedding process, are presented. In all figures the flow is from the left to the right. Note that the time step between successive images may vary in order to capture the most important instants during the process.

Fig. 9 shows the collapse of a small cavitation cloud inside a bulk liquid. This is the most ideal situation, where there are no vapour structures downstream of the cloud.

The sequence in Fig. 9 starts just before a detached cavitation cloud collapses. This occurs at t = 25 μs. The pressure builds up and reaches the magnitude in the order of 1.5 MPa. The wave then spreads symmetrically in all directions. The part of the wave, which travels upstream is immediately attenuated as it reaches the attached cavity structure. This occurs due to the nature of a highly compressible two phase mixture. The part of the wave which progresses into the bulk

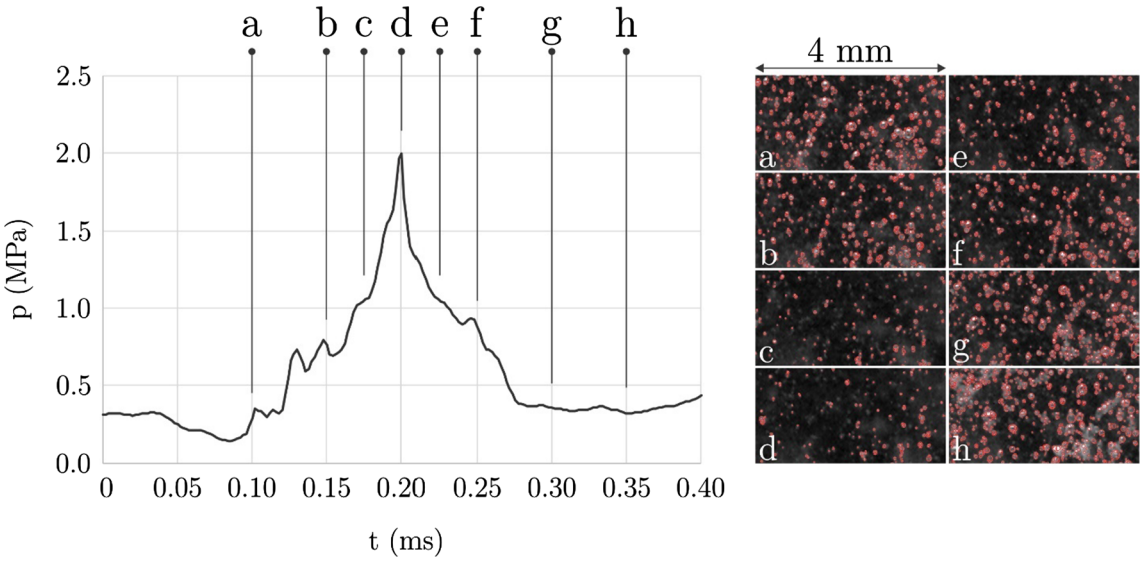

Fig. 5. Pressure recorded by the pressure transducer (left) and a synchronised closeup of the shock wave passage as recorded by the high-speed camera (right).

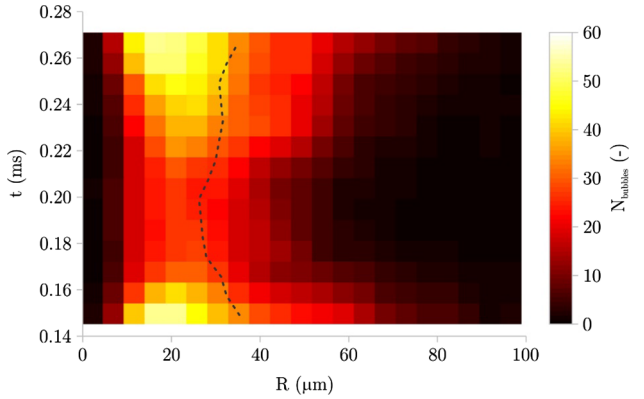

Fig. 6. Histogram of bubble size and number distribution as a response to the passage of the shock wave. The dotted line shows the average bubble size.

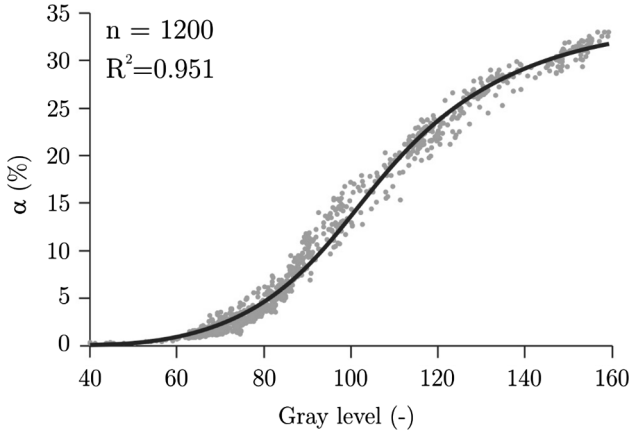

Fig. 7. Correlation between void fraction (obtained from the high-resolution images, Eq. (12)) and the local grey level (obtained from the low-resolution images). Based on 1200 pairs of data a fourth order polynomial relationship was determined for this specific experiment ($\alpha = a\cdot(gl)^4 + b\cdot(gl)^3 + c\cdot(gl)^2 + d\cdot(gl) + e$, a = -0.0000000011, b = −0.0000000266, c = 0.0000866979, d = -0.0077952188, e = 0.1819370476), a correlation of $R^2 = 0.951$ was obtained.

liquid phase travels further, but also diminishes at = 58 μs.

Previous studies by the present authors [24]have shown that one of the mechanisms that can lead to the occurrence of cavitation erosion is

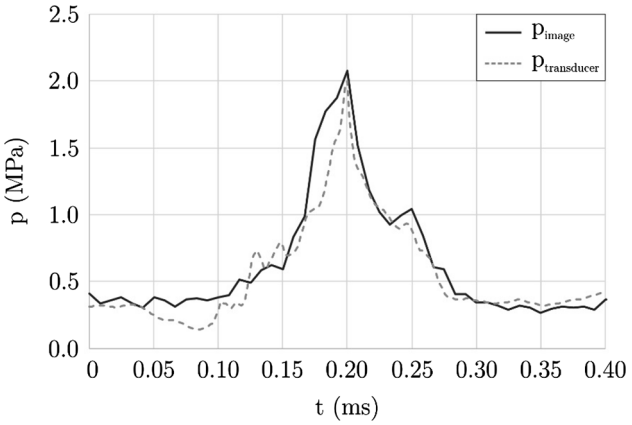

Fig. 8. Comparison of the pressure recorded by the pressure transducer and the results from image analysis.

the collapse of small vaporous structures, which occurs in the region between the attached cavity and separated cloud, just after its separation. Fig. 10 shows such a situation.

The pressure amplitude reaches approximately 1.8 MPa (at t = 33 μs). The wave then circularly spreads and is quickly attenuated as it reaches the two phase region, which surrounds it. By the time that the shock reaches the surface of the Venturi its amplitude decreases to less than 0.5 MPa, which is likely not sufficient to cause aggressive collapse of single bubbles, which would consequently cause erosion [25]. This is also in line with observations of cavitation erosion in this region [24], which showed marginal, yet measurable, occurrence of damage.

An interesting situation occurs when a small cavity separates and collapses just after a larger one detached. Here the shock wave is “trapped” between two structures, which are highly compressible (Fig. 11).

The origin of the shock wave is near the upper wall of the Venturi section, hence it spreads in a semi circular pattern. When the wave reaches the bottom Venturi wall (t = 25 μs) it separates into two parts (t = 33 μs). The one that travels upstream is completely attenuated by the attached cavity (t = 42 μs). The part which travels downstream catches the separated cavitation cloud (t = 67 μs) and shortly afterwards diminishes inside it (t = 108 μs).

The largest amplitude of the pressure wave was measured when a large cavitation cloud collapsed in a nearly pure liquid region (Fig. 12).

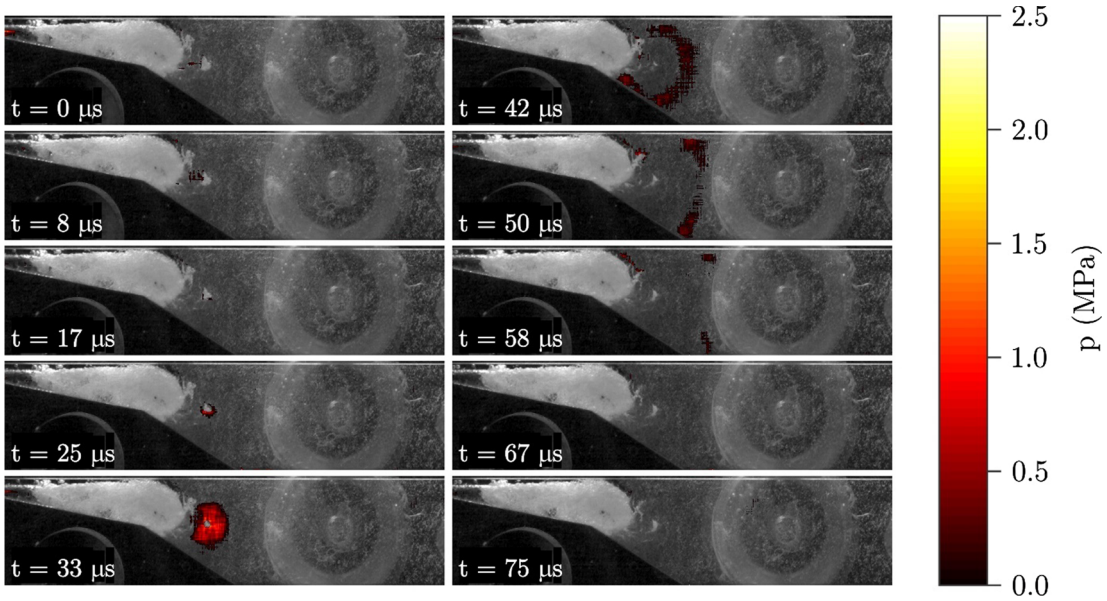

Fig. 9. Shock wave emitted at cloud collapse in the bulk flow.

In the sequence, shown in Fig. 12, at t = 8 µs, the maximal local pressure momentarily exceeded 5 MPa (we have kept the colormap scale maximum at 2.5 MPa, for the sake of better visualization of the consequent passing of the wave and also for easier comparison with other diagrams). The wave firstly forms a circular pattern, which engulfs the whole cross-section of the Venturi (t = 17 µs). It then separates into the upstream and downstream traveling parts (t = 25 µs). The former hits the attached cavity and is attenuated by it (t = 33 µs). The latter part travels downstream and still has the magnitude of 1 MPa shortly before it exits the window of observation (t = 75 µs). Approximately 10 mm downstream of the observation window the test section begins to contract to fit the connection pipe. At this plane the pressure wave reflects, travels upstream and reappears in the observation window at t = 142 µs. The wave now moves in a bubbly flow medium – the compressibility is again high and the sonic velocity correspondingly low. The wave slowly progresses upstream, where it interacts with a newly separated cavitation cloud (t = 317 µs). The middle part of the wave is attenuated inside the cloud, while the upper and lower part pass it and diminish further upstream when they enter the attached cavity.

Finally, a sequence of multiple collapses and shock reflections is shown in Fig. 13.

The first collapse can be seen at t = 0 µs. In the region, where it occurs, a high number density of bubbles is present (likely remaining there from the previous cycle of cloud separation). These contribute to the high attenuation, due to which the majority of the wave is attenuated by t = 67 µs. At this point, however, a secondary collapse occurs which releases a higher amplitude (approximately 2.5 MPa) pressure wave. Yet also this wave is rapidly attenuated by the highly compressible two-phase bubbly medium. The part which travels downstream exits the window of observation (t = 200 µs), too weak to reflect. The upstream traveling part, very similarly to the previous case (Fig. 12), interacts with the small cavitation structure (t = 233 µs).

4.3. Shock wave speed analysis

An interesting further analysis of the data are the velocities at which the shock wave travels.

The theoretical sonic velocity c_{th} was derived by Brennen [26] and

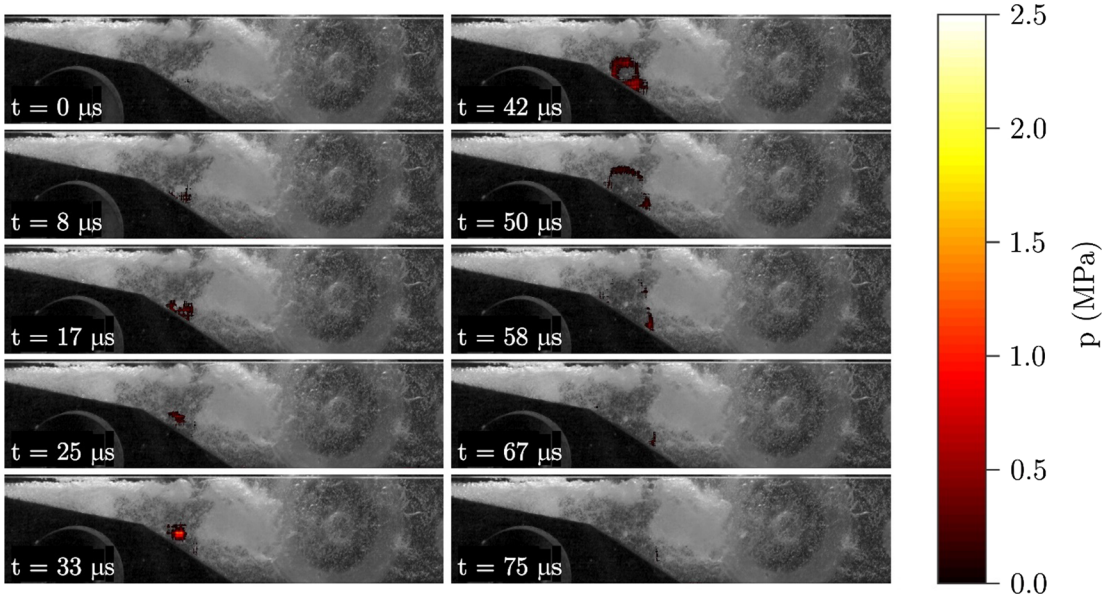

Fig. 10. Shock wave emitted beneath a vaporous cloud.

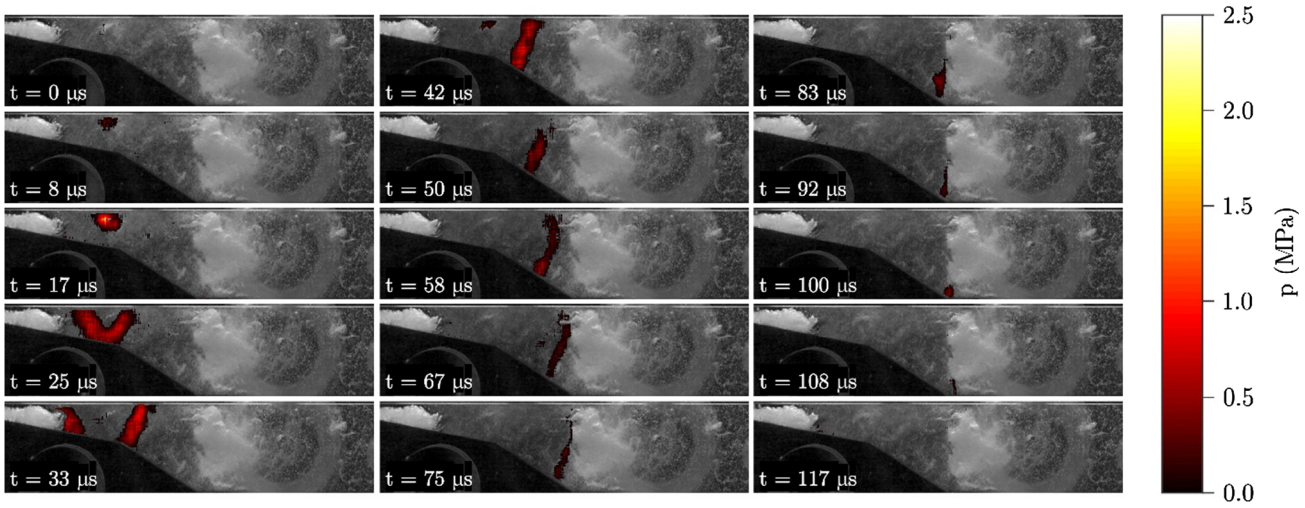

Fig. 11. Shock wave emitted in a region between attached cavity and cavitation cloud.

was further tested by Shamsborhan et al. [27]. It is highly dependent on the local void fraction α:

$$c_{th} = \left[(\rho_l(1-\alpha) + \rho_v\alpha)\left(\frac{\alpha}{np} + \frac{1-\alpha}{\rho_l c_l^2}\right)\right]^{-\frac{1}{2}} \quad (13)$$

where, ρ_l is the liquid density, ρ_v is the vapour density, n is the polytropic constant, p the local absolute pressure and c_l, the sonic velocity in pure liquid. According to Eq. (13) the theoretical sonic velocity will lie between $c_{th} = 1480$ m/s for pure liquid ($\alpha = 0\%$) and $c_{th} = 50$ m/s ($\alpha = 35\%$), which was the highest measurable void fraction in the present experiment (Fig. 7)

The following two diagrams were plotted by averaging the pressure values along the y coordinate. They correspond to the sequences shown in Figs. 11 and 12, respectively. x = 0 mm corresponds to the beginning of the observation window. The collapse occurs at t = 0 μs. The gradient of the maximum values of pressure also defines the velocity at which the pressure front moves ($c = \frac{\Delta x}{\Delta t}$) – these are noted in the figures.

Fig. 14 corresponds to the sequence presented in Fig. 11, where the shock wave is emitted in a region between attached cavity and cavitation cloud.

The origin of the pressure wave is at x = 18 mm and t = 0 μs. The wave then spreads, what can be seen as two distinctive maximal pressure lines (i) and (ii). (i) moves upstream towards the attached cavity and is engulfed by it at x ≈ 10 mm and t ≈ 33 μs. the other front (ii) goes in the same direction as the flow and reaches the separated cavitation cloud at x ≈ 35 mm and t ≈ 60 μs (it is completely attenuated at t ≈ 100 μs). The region near the attached cavity seems to be populated by somewhat smaller number of bubbles, what results in a higher velocity of front movement $c_i = 431$ m/s. The front moving in the other direction has a velocity of $c_{ii} = 267$ m/s.

Fig. 15 corresponds to the sequence presented in Fig. 12, where the shock wave emission and reflection was observed.

The cavitation cloud collapses at x = 34 mm and t = 0 μs. Again, the pressure wave spreads in all directions what can be seen as two maximum pressure lines (iii) and (vi) with the same origin. The cloud collapsed relatively far away from either attached cavity or the previously separated cavitation cloud, hence the medium in the vicinity is relatively homogeneous. This results in almost equal velocities of both upstream (iii) and downstream (iv) going fronts – $c_{iii} = 532$ m/s and $c_{iv} = 524$ m/s, respectively. The upstream from (iii) is almost completely attenuated as it reaches the attached cavity at x = 11 mm and t ≈ 30 μs. However, what could not be seen in Fig. 12, a very weak reflection occurs (v). The front moves at a very high velocity of $c_v = 704$ m/s. This points to the fact that very small volume of free gas is present in this region, which is a result of the prior passage of the primary pressure wave (iii). The wave traveling downstream (iv) leaves the observation window and reflects. The reflected shock (vi) travels relatively slowly $c_{vi} = 178$ m/s. This, again, is expected. A part of the

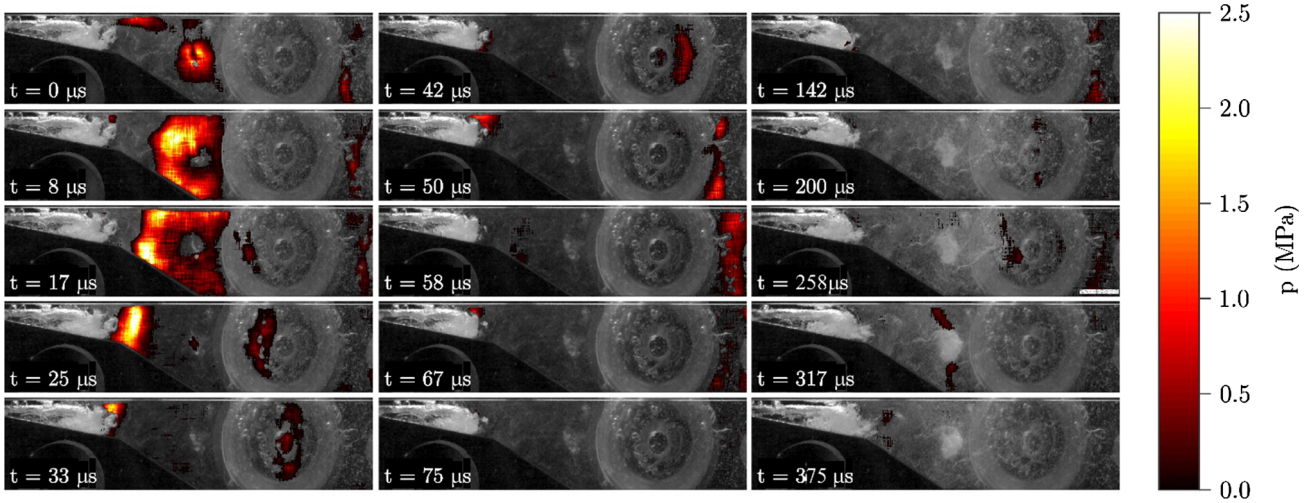

Fig. 12. Shock wave emission and reflection at the convergence downstream of the test section.

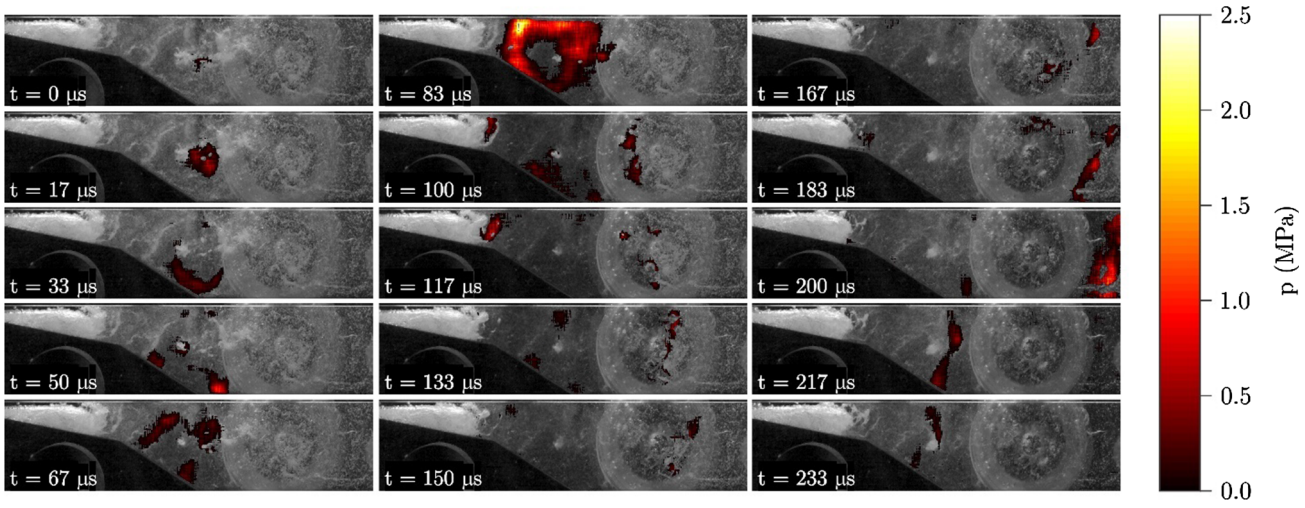

Fig. 13. Primary and secondary shock waves.

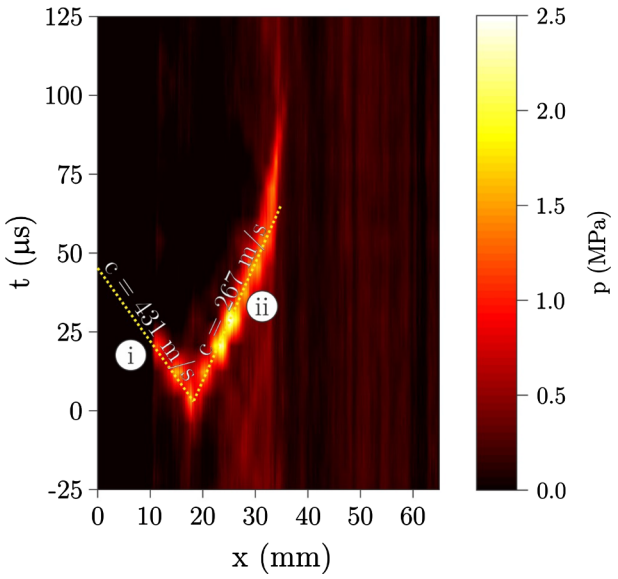

Fig. 14. Averaged shock wave profile for case in Fig. 11.

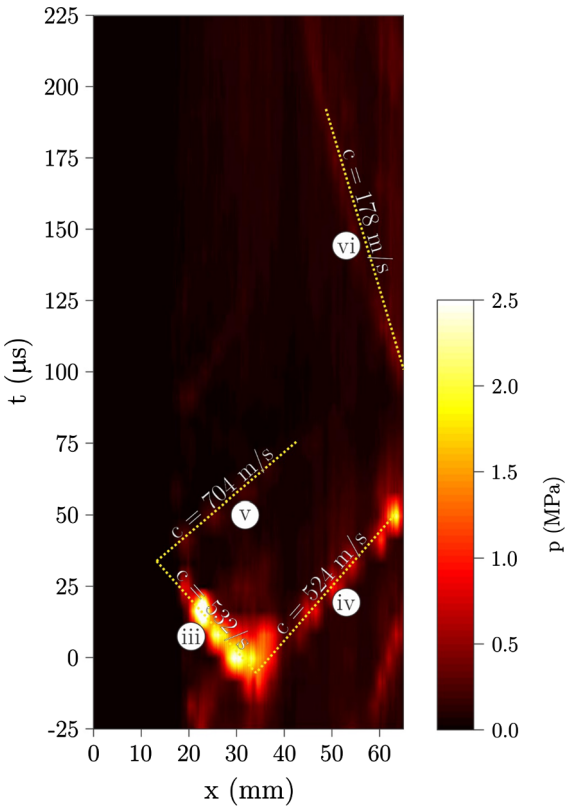

Fig. 15. Averaged shock wave profile for case in Fig. 12.

cavitation cloud "survived" the collapse (see Fig. 12), hence the region, through which the wave (vi) travels, is seeded by bubbles, what decreases the local sonic velocity.

The flow, especially the one in the vicinity of the throat of the Venturi is highly compressible. Also, inside the cavity, the pressure is low, what results in very low local sonic velocity - in the order of several m/s. This of course results in a fact, that we are dealing with a supersonic flow conditions [4], which means that the pressure waves travel at Ma ≫ 1.

Looking at the raw images and the correlation between the local void fraction α and the grey level (Fig. 7) we can approximately determine the local theoretical sonic velocity c_{th} (Eq. (13)).

Table 1 shows the results together with the Mach numbers ($Ma = \frac{c}{c_{th}}$) of individual front from Figs. 14 and 15. Of course, these values serve only as a rough estimate, since the method of determining α is not precise and c_{th} is highly dependent on it (the uncertainty of Ma number value in Table 1 bases mainly on the accuracy of measurement of α).

Obviously, in all cases the front travels at a supersonic velocity, exceeding it by a factor 2 or even more. Again, we stress that the values, listed in the table are only rough estimates, but they do evidently show that we are dealing with supersonic shock waves in cavitating flow. This is also in line with observations, recently made by Ganesh et al. [4] and Ganesh et al. [5].

5. Conclusions

This study shows an option of detecting and evaluating shock waves inside the cavitating flow with conventional high-speed visualization. In order to get reliable results, both resolution and frequency of visualization must be relatively high. The presented method was tested on a simple Venturi constriction, where intense cavitation cloud shedding was established. The method was calibrated by reference pressure pulsation measurement conducted by high frequency pressure transducer, which was installed directly into the flow channel. Calibration

Table 1
Void fraction, pressure front velocity, theoretical sonic velocity for cases shown in Figs. 14 and 15.

Pressure front	α (%)	c (m/s)	c_{th} (m/s)	Ma (–)
i	2.5	431	177	2.4 ± 0.7
ii	8.3	267	101	2.7 ± 0.2
iii	1.5	532	228	2.3 ± 0.7
iv	2.1	524	193	2.7 ± 0.9
v	0.4	704	425	1.7 ± 1.2
vi	21.3	178	68	2.6 ± 0.1

depends on visual perception of small bubbles in the flow, where the bubbles shrink when shock wave passes them.

This relatively simple approach enabled the first observation of shockwaves which occur at the cavitation cloud collapse (downstream of the attached cavity). Presented study distinguishes various cases of shock waves formation:

- Cavitation cloud collapse inside the bulk liquid causes omnidirectional pressure wave, if it is strong enough the downstream front can reflect from the end of test section back upstream.
- Shock wave emitted beneath a vaporous cloud is rapidly attenuated when it reaches the high void fraction region.
- Shock wave emitted between attached cavity and separated cavitation cloud is attenuated when reaching two phase regions.
- Cloud collapse causes primary shock wave formation which can later on trigger additional cloud collapse and releasing secondary shock wave.

Pressure wave analysis estimates maximal local pressures caused by cavitation cloud collapse in order of several MPa, in some cases, momentarily exceeding 5 MPa.

Shock wave speed analysis showed that the fronts, downstream of the attached cavity, can move with extremely high velocities, which also depend on the local bubble population. Comparing shock wave fronts movement velocities with theoretical sonic velocities for individual void fraction regions, one can clearly determine supersonic movement with Mach number exceeding 2.

CRediT authorship contribution statement

Martin Petkovšek: Investigation. **Marko Hočevar:** Investigation, Writing - review & editing. **Matevž Dular:** Conceptualization, Methodology, Visualization, Writing - review & editing, Supervision.

Declaration of Competing Interest

The authors declare that they have no known competing financial interests or personal relationships that could have appeared to influence the work reported in this paper.

Acknowledgements

The authors acknowledge the financial support from the Slovenian Research Agency (research core Funding No. P2-0401 and J7-1814) and the European Research Council (ERC) under the European Union's Framework Program for research and innovation, Horizon 2020 (grant agreement n° 771567 - CABUM).

References

[1] M. Dular, R. Bachert, B. Stoffel, B. Širok, Experimental evaluation of numerical simulation of cavitating flow around hydrofoil, European Journal of Mechanics B/Fluids 24 (2005) 522–538.
[2] M. Dular, R. Bachert, C. Schaad, B. Stoffel, Investigation of a re-entrant jet reflection at an inclined cavity closure line, Eur. J. Mech. B/Fluids 26 (2007) 688–705.
[3] Y.-C. Wang, C.E. Brennen, Shock Wave Development in the Collapse of a Cloud of Bubbles, Asme 211 (1994) 15–19.
[4] H. Ganesh, S.A. Mäkiharju, S.L. Ceccio, Bubbly shock propagation as a mechanism for sheet-to-cloud transition of partial cavities, J. Fluid Mech. 802 (2016) 37–78.
[5] H. Ganesh, S.A. Mäkiharju, S.L. Ceccio, Bubbly shock propagation as a mechanism of shedding in separated cavitating flows, J. Hydrodynam. 29 (6) (2017) 907–916.
[6] M. Bhatt, K. Mahesh, Numerical investigation of partial cavitation regimes over a wedge using large eddy simulation, Int. J. Multiph. Flow 122 (2020) 103155.
[7] B. Budich, S.J. Schmidt, N.A. Adams, Numerical simulation and analysis of condensation shocks in cavitating flow, J. Fluid Mech. 838 (2018) 759–813.
[8] C.F. Delale, Bubble dynamics and shock waves. Bubble Dynamics and Shock Waves, Springer Berlin Heidelberg, 2013. doi:10.1007/978-3-642-34297-4.
[9] R. Petkovšek, J. Možina, G. Močnik, Optodynamic characterization of shock waves after laser-induced breakdown in water, Opt. Express 13 (11) (2005) 4107–4112.
[10] R. Petkovšek, P. Gregorčič, A laser probe measurement of cavitation bubble dynamics improved by shock wave detection and compared to shadow photography, 2007. doi:10.1063/1.2774000.
[11] O. Supponen, D. Obreschkow, P. Kobel, M. Tinguely, N. Dorsaz, M. Farhat, Shock waves from nonspherical cavitation bubbles, Phys. Rev. Fluids 2 (9) (2017) 093601.
[12] C.E. Brennen, G. Reisman, Y.C. Wang, Shock Waves in Cloud Cavitation, Proceedings of the Twenty First Symposium on Naval Hydrodynamics, 1992, pp. 756–771.
[13] E.A. Brujan, T. Ikeda, Y. Matsumoto, Shock wave emission from a cloud of bubbles, Soft Matter 8 (2012) 5777.
[14] Y. Sugimoto, K. Sato, S. Oojimi, Visualization of pressure wave generated by collapse of cavitation cloud using frame difference method, 2008, pp. 1–10.
[15] M. Waldrop, F. Thomas, Video: Shock Wave Propagation: Cavitation of Dodecane in a Converging-Diverging Nozzle, in: 68th Annual Meeting of the APS Division of Fluid Dynamics - Gallery of Fluid Motion, American Physical Society, 2015. doi:10.1103/APS.DFD.2015.GFM.V0027.
[16] U. Rasthofer, F. Wermelinger, P. Hadijdoukas, P. Koumoutsakos, Large Scale Simulation of Cloud Cavitation Collapse, Proc. Comput. Sci. 108 (2017) 1763–1772.
[17] W. Jian, M. Petkovšek, L. Houlin, B. Širok, M. Dular, Combined numerical and experimental investigation of the cavitation erosion process, J. Fluids Eng., Trans. ASME 137 (5) (2015), https://doi.org/10.1115/1.4029533.
[18] M. Dular, T. Griessler-Bulc, I. Gutierrez-Aguirre, B. Kompare, Use of hydrodynamic cavitation in (waste)water treatment, Ultrason. Sonochem. 29 (2016) 577–588.
[19] M. Zupanc, T. Kosjek, M. Petkovšek, M. Dular, B. Kompare, B. Širok, Ž. Blažeka, E. Heath, Removal of pharmaceuticals from wastewater by biological processes, hydrodynamic cavitation and UV treatment, Ultrason. Sonochem. 20 (4) (2013) 1104–1112, https://doi.org/10.1016/j.ultsonch.2012.12.003.
[20] A. Šarc, T. Stepišnik-Perdih, M. Petkovšek, M. Dular, The issue of cavitation number value in studies of water treatment by hydrodynamic cavitation, Ultrason. Sonochem. 34 (2017) 51–59.
[21] B. Bizjan, A. Orbanić, B. Širok, B. Kovač, T. Bajcar, I. Kavkler, A computer-aided visualization method for flow analysis, Flow Meas. Instrum. 38 (2014) 1–8.
[22] M. Dular, O. Coutier-Delgosha, Thermodynamic Effects during the Growth and Collapse of a Single Cavitation Bubble, J. Fluid Mech 736 (December) (2013) 44–66.
[23] M. Dular, B. Bachert, B. Stoffel, B. Širok, Relationship between cavitation structures and cavitation damage, Wear 257 (11) (2004) 1176–1184.
[24] M. Dular, M. Petkovšek, On the mechanisms of cavitation erosion - Coupling high speed videos to damage patterns, Exp. Therm Fluid Sci. 68 (2015) 359–370.
[25] M. Dular, T. Požar, J. Zevnik, R. Petkovšek, High speed observation of damage created by a collapse of a single cavitation bubble, Wear 418–419 (2019) 13–23.
[26] C.E. Brennen, Cavitation and Bubble Dynamics, Oxford University Press, Pasadena, California, 1995.
[27] H. Shamsborhan, O. Coutier-Delgosha, G. Caignaert, F. Abdel Nour, Experimental determination of the speed of sound in cavitating flows, Exp. Fluids 49 (6) (2010) 1359–1373.